CORA Cork Open Research Archive
Cartlann Taighde Oscailte Chorcaí

Title	Layered graphitic carbon host formation during liquid-free solid state growth of metal pyrophosphates
Authors	Díaz, Carlos;Valenzuela, María Luisa;Lavayen, Vladimir;O'Dwyer, Colm
Publication date	2012-05-15
Original Citation	Diaz, C., Valenzuela, M. L., Lavayen, V. and O'Dwyer, C. (2012) 'Layered graphitic carbon host formation during liquid-free solid state growth of metal pyrophosphates', Inorganic Chemistry, 51(11), pp 6228–6236. http://dx.doi.org/10.1021/ic300767h
Type of publication	Article (peer-reviewed)
Link to publisher's version	10.1021/ic300767h
Rights	© 2012 American Chemical Society. This document is the Accepted Manuscript version of a Published Work that appeared in final form in Inorganic Chemistry, copyright © American Chemical Society after peer review and technical editing by the publisher. To access the final edited and published work see http://pubs.acs.org/doi/abs/10.1021/ic300767h
Download date	2026-11-05 22:42:16
Item downloaded from	https://hdl.handle.net/10468/2808

UCC
University College Cork, Ireland
Coláiste na hOllscoile Corcaigh

Layered Graphitic Carbon Host Formation during Liquid-free Solid State Growth of Metal Pyrophosphates

Carlos Díaz[1*], María Luisa Valenzuela[2], Vladimir Lavayen[3], and Colm O'Dwyer[4,5†‡]

[1] *Department of Chemistry, Faculty of Science, Universidad of Chile, Casilla 653, Santiago, Chile*
[2] *Universidad Andres Bello, Facultad de Ciencias Exactas, Departamento de Ciencias Quimicas. Av. Republica 275, Santiago, Chile.*
[3] *Faculdade de Química, Pontifícia Universidade Católica do Rio Grande do Sul, Porto Alegre - RS CEP 90619-900, Brazil*
[4] *Department of Physics and Energy, University of Limerick, Limerick, Ireland*
[5] *Materials and Surface Science Institute, University of Limerick, Limerick, Ireland*

Abstract

We report a successful ligand- and liquid-free solid state route to form metal pyrophosphates within a graphitic carbon matrix through a single step approach involving pyrolysis of previously synthesized organometallic derivatives of a cyclotriphosphazene. In this case, we show how single crystal $Mn_2P_2O_7$ can be formed either on the micro- or nanoscale in the complete absence of solvents or solutions by an efficient combustion process using rationally designed macromolecular trimer precursors, and present evidence and a mechanism for layered graphite host formation. Using *in situ* Raman spectroscopy, infrared spectroscopy, X-ray diffraction, high resolution electron microscopy, thermogravimetric and differential scanning calorimetric analysis, and near-edge X-ray absorption fine structure examination, we show evidence for the formation of a layered, graphitic carbon in the matrix and how the process occurs. The identification of thermally and electrically conductive graphitic carbon host formation is important for the further development of this general ligand-free synthetic approach for inorganic nanocrystal growth in the solid state, and can be extended to form a range of transition metals pyrophosphates. For important energy storage applications, the method gives the ability to form oxide and (pyro)phosphates within a conductive, intercalation possible, graphitic carbon as host-guest composites directly on substrates for high rate Li-ion battery and emerging alternative positive electrode materials.

[*] Email: cdiaz@uchile.cl
[†] Email: colm.odwyer@ul.ie
[‡] Present address: Department of Chemistry, University College Cork, Cork, Ireland, and Tyndall National Institute, Lee Maltings, Cork, Ireland

1. Introduction

Graphitic carbonaceous materials, including nanohorns, nanorods, nanofibers, nanocages, and of course nanotubes[1], fullerenes and graphene[2] have a number of definitive uses including their application in electrical and thermal devices, as adsorbent, sieving and storage media including H_2 storage, and as catalytic supports, due of their unique chemical and physical properties[3-5]. The recent development of graphitic foams[6] characterized by highly aligned graphitic structures has attracted attention for thermal management devices[7], and with unusually high thermal conductivity-to-weight ratios such graphitic carbons are promising aeronautical and aerospace industrial materials. Among the many methods for carbon nanostructure growth[8-10], the organometallic approach[11-13] has been widely used and is one of the principal synthetic methods. The organometallic compound involves the pyrolysis of the precursors at elevated temperatures under a N_2 atmosphere or vacuum[12]. Typically, the metal catalyzes the transformation of the organic matter to graphitic materials. Cage-like carbons, for example, have been fabricated by a template method where carbon shells encapsulated with Fe particles were first generated by laser-induction complex heating evaporation, followed by removal of the catalyst with an inorganic acid[14]. Such carbons are analogous to cyclomatrices formed during thermolysis of carbon containing liquids, solvents and polymers.

While the plethora of carbon and graphitic nanostructures owe their synthetic origins to many metallic catalysts and associated reactions, carbons can also influence the growth of metallic structures. There are many known methods for preparing metallic nanostructures, and solution-based methods have been the most prevalent, owing to the relatively simple chemistries involved in reducing metallic salts in appropriate solvents[15-17]. By comparison, relatively few solid-state strategies for pure metallic nanostructured materials have been reported[18-22]. In recent work[23-29], we reported a new solid-state method allowing the formation of metallic (M), oxidic (M_xO_y) and (pyro)phosphate-based ($M_xP_yO_z$) nanostructured materials without necessitating liquids or solutions. Detailed investigations have shown that the resulting structures and their shapes strongly depend on the metal used, which can be a noble, transition or valve metal, and also on the molecular precursors to which the metal centers are coordinated. The strategy involves the design and pyrolysis of organometallic derivatives of poly- and cyclotriphosphazenes with coordinated metals that allows the formation of the resulting metallic nanomaterials, as summarized in Scheme 1 below.

Another aspect of this approach is that the composition and the morphology of the pyrolytic products are also sensitively dependent on the structure of the organometallic precursors. Because of this overarching dependence, and the fact that a wide range of materials and shapes are possible through precursor design, information is needed on the complex thermal decomposition processes as a function of the precursor structure and its resulting influence on the growth of the inorganic phase. Here, we explore the general mechanism for this overall solid state strategy and specifically detail the formation and mechanism of layered graphitic carbon formation inside which the crystalline nanomaterials are formed. The mechanism of formation of nanoparticles in solution is now very well advanced[30-35], and significant insight into the solid state precursor-mediated method can be extracted from the formation of these nanomaterials, including the influence of the host matrix on the crystal growth of the non-carbonaceous phase. This was recently demonstrated by Tannenbaum *et al.*[35] in the solid state preparation of metallic nanoparticles embedded in polymer. More recently, the pyrophosphates and phosphates which can result from the precursors by our method, have been investigated within the last year[36] as useful Li-ion battery materials and this approach augers well for the creation of a wide variety of transition metal-based pyrophosphates as tunnel-structure intercalation hosts for battery materials and energy storage. By this solid state approach, conductive layered, conductive graphitic carbon additives are formed in intimate contact with intercalation-possible inorganic (pyro)phosphate and oxide crystals directly on substrates; a one-step battery composite material without any liquid-based synthetic steps.

For the solid state method outlined in Scheme 1, we have proposed a mechanism principally based on thermogravimetric (TG) and differential scanning calorimetric (DSC) studies of precursor pyrolysis. This mechanism is outlined in Scheme 2.

The first step involves the cross-linking of the polymer chains or the trimer to create a 3-D network or matrix. As previously shown[24], this step is essential in preventing the volatilization of the sample on heating. The second step involves carbonization of the organic matter. This step produces the CO/CO_2 mixtures; these gaseous products form holes in a thermally decomposing polymer and allow the agglomeration of cleaved metallic centers from the precursor to ripen into metallic nanoparticles. The formation of metal oxide nanoparticles can then occur in two steps: (1) Oxidation of the previously formed metal with a neutral oxidation state, which can occur in the presence of O_2 from reduction of CO/CO_2 mixtures and the corresponding M^0 ion, and (2) direct reaction of the M^{+n} ion (n = valence state) with O_2:

$$M^0 + O_2 \longrightarrow M_xO_y \quad (1)$$

$$M^{+n} + O_2 \longrightarrow M_xO_y \quad (2)$$

On the other hand, metal pyrophosphate nanostructured salts can be formed by simple reaction of the M^{+n} ions (as in the case of Mn in Scheme 1) with the *in situ* formed pyrophosphate anions from oxidation of the phosphazene P atoms:

$$M^{+n} + P_2O_7^{2-} \longrightarrow M_x(P_2O_7)_y \quad (3)$$

In all cases a low metal/P,N ratio produces P_4O_7 or P_4O_9 molecules in excess which act as a stabilizing matrix for the nanoparticles. The step involving the carbonization of the organic matter is expected to form some carbonaceous material, at intermediate temperatures. To investigate the composition and structure of the important carbon host matrix, we report detailed *in situ* heated Raman scattering, FTIR, SEM-EDAX, HRTEM and TG/DSC studies of the solid-state pyrolysis of trimer (**1**), reproduced in Fig. 1 below, and we show that the pyrolytic decomposition mechanism of the precursor results in a layered, graphitic carbon matrix where metal, metal oxide and metal pyrophosphate nanostructures can form, and this work shows that it is mediated by the conversion of an initially amorphous matrix to polycrystalline graphitic carbon. The findings are generally applicable to the many solid state precursors so far investigated.

2. Experimental section

2.1 Precursor

The compound $\{NP(OC_8H_{12})_2(OC_6H_4PPh_2\text{-}Mn(CO)_2(\eta^5\text{-}C_5H_4Me)_2\}$ **(1)** was prepared as previously reported[37].

2.2. Pyrolysis

The pyrolysis experiments were made by pouring a weighed portion (0.05–0.15 g) of the precursor trimer **(1)** into aluminum oxide boats that were placed in a furnace (Daihan oven model Wise Therm FHP-12) under a flow of air, heating from 25°C to upper temperature limits of 250°C, 300°C, 315°C, 325°C, 400°C, 600 °C and 800 °C, followed by annealing for 2 h in each case. The heating rate was consistently maintained at 10 °C min^{-1} for all experiments.

2.3. Characterization of the pyrolytic samples

Solid pyrolytic samples were characterized by scanning electron microscopy (SEM), high resolution transmission electron microscopy (HRTEM), Fourier transform infra-red (FTIR) spectroscopy, Raman scattering spectroscopy and thermogravimetric (TG) and differential scanning calorimetric (DSC) analysis. SEM images were acquired with a Philips EM 300 scanning electron microscope. Energy dispersive X-ray analysis (EDAX) was performed on a NORAN Instrument micro-probe attached to a JEOL 5410 scanning electron microscope. TEM data were acquired using a JEOL SX100 and a JEOL 2011 transmission electron microscope. The TEM samples were prepared by dispersing pyrolized material onto copper grids and dried at room temperature. For high resolution examination of graphitic carbons, flakes of sonicated carbons were dispersed on grids and examined under SEM to determine their thickness. Graphitic samples were left intentionally >100 nm thick to compensate for beam damage to the exposed surface.

X-ray diffraction (XRD) was conducted at room temperature on a Siemens D-5000 diffractometer with θ-2θ geometry. The XRD data was collected using Cu-Kα radiation (40 kV, 30 mA). FTIR measurements were performed on a Perkin Elmer FTIR spectrophotometer model Spectrum BXII. Raman scattering measurements were performed on a Renishaw Raman Microscope System RM1000 equipped with a 2.41 eV laser line. The output laser power was maintained in the range 10-100 mW, resulting in maximum laser power densities < 10^7 W cm^{-2}.

TGA and DSC measurements were performed on a Mettler TA 4000 instrument and Mettler DSC 300 differential scanning calorimeter, respectively. The trimer samples were heated at a rate of 10 ºC min^{-1} from ambient temperature to 1000 ºC under a constant flow of nitrogen.

Near-edge X-ray absorption fine structure (NEXAFS) measurements were carried out at the PM-3 beam-line of the BESSY Synchrotron Radiation Facility in Berlin, Germany. Thin film deposits of the carbon material pyrolyzed to 800 °C were examined on metallized silicon substrates. NEXAFS spectra at the carbon and oxygen K-edges were measured. Data were captured with surface sensitive total electron yield at an angle of incidence of 45° and were normalized to separate measurements of the metallized substrate.

3. Results and Discussion

3.1 Crystal growth during initial pyrolysis

Pyrolysis of the complex precursor **(1)** under air and at 800 °C results in a white solid identified by powder XRD, shown in Fig. 2a, as $Mn_2P_2O_7$ (ICDD File No. 29-0891). Similar single crystal pyrolytic products were obtained from the pyrolysis of the trimer compound $\{NP(OC_6H_4PPh_2\text{-}Mn(CO)_2(\eta^5\text{-}C_5H_4Me)_6\}$ as well as from the analogous polymer[38] and related systems. The material is a porous solid; the solid regions comprise the pyrolyzed single crystal materials interspersed with voids or pores akin to disordered mesoporous materials. Acounting for known size distributions in the Scherrer constant or by estimating variances from a unimodal distribution using Warren-Averbach approaches to the Fourier transform of XRD data does not confirm the size distribution and the best estimates are found from large area TEM images acquired at high angle to maximize contrast from the higher scattering $Mn_2P_2O_7$ (compared to carbon). The XRD pattern in Fig. 2a also displays a broad peak centered at approximately 26° 2θ, from the (002) reflection of graphite with a corresponding spacing between planes of carbon of ~0.34 nm. The appearance of this broad peak indicates that the initial amorphous structure of the carbonized organic matter becomes more ordered during intermediate pyrolysis temperatures as the carbon converts to graphitic carbon.

The morphology of the product is that of a porous matrix that contains the $Mn_2P_2O_7$ crystals, as is shown in Fig. 2b. EDAX analysis (Fig. 2c) confirms the presence of mainly Mn, P, C and O. As this material is analyzed after full pyrolysis and annealing at 800 °C, the resulting quantity of carbon is quite small compared to intermediate stages, shown further on. TEM analysis of some of the crystalline material shows that it is primarily composed of irregular crystals with a broad size distribution as shown in Fig. 2d. Particles with sizes in the range 200 – 450 nm are typically observed, confirming global estimates from XRD data. The size distribution in Fig. 2e confirms a log-normal variation of particle sizes, accounting for asphericity in microscopy images.

3.2 Raman scattering and vibrational spectroscopy of decomposition and graphitization

Since the formation of the nanoparticles and crystals depends on several key steps such as 1) the thermal dewetting characteristics of the solidifying polymer and its influence on nanoscale seed particle coarsening by solid stage diffusion barriers, 2) cleavage of metal centres so that aggregation occurs to seed metallic crystals (and subsequent oxidation for oxides), which incubate in the porous carbonizing host, and 3) the composition and crystallinity of the matrix in which the particles grow, we investigated the intermediate temperatures during pyrolysis to clarify the matrix

structure and composition. For nanoparticles to form, it is known that carbonaceous matrices require higher temperatures than oxides for metallic nanoparticle seed ripening to occur, owing to the high thermal conductivity of the carbon[39,40]. Using IR absorbance, we monitored the molecular vibrations of the νCO region of the cymantrene[39] groups of precursor **(1)** during pyrolytic annealing at several temperatures, shown in Fig. 3. On heating from 250 to 400 °C, we observe the complete disappearance of the νCO bands from the cymantrene groups. The progressive decrease of the two absorption bands of the $Mn(CO)_2$ moiety, and the fact that we never observe the single band corresponding to the Mn(CO) moiety, suggests the simultaneous loss of the two carbonyls contrary to what is expected through a step-by-step loss of one CO and then the second[37, 38]. This agrees with the mechanism proposed for the formation of nanostructured materials from solid precursors and suggests that volatile components are easily ejected from the matrix during intermediate steps.

The changes in compound **(1)** on annealing were also investigated by *in situ* Raman scattering spectroscopy at several temperatures. As shown in Fig. 4a, the characteristic D and G bands of graphite[41-43] (1000-1600 cm^{-1}) are found at all laser power densities (LPD) for a sample that previously underwent constant heating at 400 °C. The D-band is attributed to defects, curved graphite sheets, and lattice distortions in carbon structures, and the G-band is characteristic of graphite[44-47]. Experimental annealing temperatures are calculated from Stokes/anti-Stokes components of the Raman spectra from the peak positions of the Stokes (ω_S) and anti-Stokes (ω_{AS}) components according to $n(\omega_S)I_S = \{n(\omega_{AS}) + 1\}I_{AS}$, where I_S and I_{AS} are, respectively, the cross sections of the Stokes and anti-Stokes components for each measurement, and $n(\omega) = 1/[\exp(\hbar\,\omega/k_BT) - 1]$ is the Bose-Einstein thermal factor, T is the sample temperature, and k_B is Boltzmann's constant. We assume in this case that the thermal conductivity of the carbon acts as a sufficient heat sink so as to maintain a constant temperature at the region of the maximum intensity of the laser beam waist. Cançado *et al.*[48] have previously shown that 2D graphite is a poorer heat sink than 3D graphite, but the expected downshift in the G band frequency is not observed here.

The observation of the D and G bands in Raman spectra and the fact that both bands are clearly discernible is direct evidence that the decomposition process involves carbonaceous intermediates that contain polycrystalline graphite in a layered form. Deconvolution of other specific spectral bands confirms the presence of remnant

fragments containing P-CH_3 bonds. These organic moieties are typical of an incomplete step in the carbonization of the organic matter, as will be discussed further on. The G band, which usually occurs at ~1580 cm^{-1} is assigned to a graphite phonon mode often associated with single-layer graphene. The disorder-induced D band (about 1350 cm^{-1}) is a phonon associated with lattice defects as it is forbidden in perfect single layers of graphene; the intensity of the D-band has been commonly used for practical applications to evaluate the amount of disorder in carbon materials. In situ heated Raman scattering in Fig. 4 shows that the D-band position slightly shifts to lower wavenumbers as excitation power density increases to 25 mW (~10^7 W cm^{-2}).

At 514.5 nm excitation, the G band, associated with graphitic carbon[49], is located at 1595 cm^{-1} after initial decarbonylation and decomposition at 400 °C, but prior to locally induced laser power heating. The G-band shows a characteristic single Lorentzian peak, indicative of graphite, as opposed to carbon nanostructures of metallic or semiconducting nature. Additionally, the G-band downshifts in frequency during localized laser induced heating, which confirms the formation of more ordered graphitic sp^2 carbon in the intermediate stages of the trimeric decomposition. In high quality graphite, it is common to observe only the G band. Here, the G band clearly develops with increased local heating. For the D band, one of the two scattering processes is not phonon-related, but elastic scattering by a defect. Specifically, the G′ peak (~2700 cm^{-1} at 514.5 nm irradiation) appears as a doublet, which is well known to result from interlayer coupling in the case of layered carbons and graphite and contributions from 2D and 3D graphite. The G′ band corresponds to two-phonon scattering processes where defects are not needed, and is a further confirmation that the resulting carbon intermediate formed during this solid state process is graphitic. In previous studies of polyparaphenylene-based carbon[48] and HOPG, for example, differentiation between 3D and 2D graphite can be obtained from splitting in the G′ band. The carbon matrices contain some 2D and 3D graphite, as seen by HRTEM (Fig. 5) for the carbon graphitized during pyrolysis by this method. The main contribution to disorder-induced Raman scattering peaks comes from unaligned 2D graphite. For samples investigated, this misalignment is most profound in curved flakes where even the 2D graphite is disordered.

A characteristic of D and G bands from Raman spectra of graphitic carbons is the ratio of their integrated peak intensities, which gives information on the degree of graphitization of the carbon. The D-band has been used for many years to estimate the graphitic in-plane crystallite size, L_a, in disordered carbon materials, since the integrated

intensity ratio I_D/I_G is proportional to L_a^{-1} and also to the laser energy, E_{laser}[-4 6, 50, 51]. We performed measurements using predefined laser powder densities to control localized heating, for precursors pyrolyzed at 400 °C (as for Fig. 4a-c) and also after heating at 600 °C. Pyrolysis at 400 °C allowed examination of the carbonized matrix after the removal of CO_2 and CO. During the decomposition of the precursor, we observe (Fig. 4d) that the I_D/I_G ratio initially follows what is expected for thermal treatment of carbon with a decrease in the ratio (more amorphous carbon, less graphite). In Fig. 4d, the I_D/I_G ratios as a function of laser energy, measured after pyrolysis to 400 and 600 °C, follow a tendency different to that observed in other graphitization processes[42]. Typically, in graphitization processes, the I_D/I_G ratio decreases with the increasing laser energy, and scales as indicated above, particularly when disorder is introduced into the graphite. In the present case, we observe the decrease of the I_D/I_G ratio from 10 to 25 mW ($<10^7$ W cm^{-2}), followed by an increase at successively higher laser power densities for samples previously pyrolyzed at 400 and 600 °C. This behavior can be explained with the help of the scheme shown in Fig. 5. The initial decrease of I_D/I_G is interpreted as the carbonization process upon annealing, provoked here by the incident laser radiation after the trimer was pyrolyzed to cleave the metal centers from the precursor and allow crystal growth within the carbon matrix. Under normal combustion conditions, the majority of the organic material is converted to carbon at 600 °C. the slight increase with laser power confirms some disorder within the graphite, and the ultimate graphitic phase is found to be similar after laser heating of carbon formed at 400 and 600 °C; the latter attains the final graphitic phase sooner, as seen in Fig. 4d.

Not all of the organic matter is converted to carbon at these temperatures (some P-CH_3 bonds are detected among others), in spite of metal center cleavage and the initiation of inorganic nanomaterial growth within the carbon matrix. Although partially graphitized carbon phonons are observed from the matrix after heating to 400 °C, generation of CO_2 occurs (step 1, Fig. 5a), as was detailed using FTIR (Fig. 3). As seen in Fig. 4c, remnant C-O bonds are detected after laser heating for sample pyrolyzed at 400 °C, and subsequently removed with increased laser power, while the carbon is continually converted to graphite through localized Joule heating from the incident photon energy (Fig. 4b and c). After carbonization of organic matter, graphitization occurs continually with time at intermediate temperatures. At successively higher laser powers both graphite formation and organic matter decomposition occurs (steps 2 and 3) with the latter eventually dominating at T ~ 800 °C.

3.3 Structure and composition of the layered graphitic host

When the organic matter decomposes, the initial carbons are amorphous and thus the ratio of amorphous carbon to graphitic carbon in regions where the organic matter has not yet decomposed, will show an decrease in the I_D/I_G ratio upon raising the temperature by incident light. At 400 and 600 °C (Fig. 4d), this process becomes self-limiting; organic matter decomposing to amorphous carbon will subsequently convert to graphite (step 3) at higher temperatures, indicating an equilibrium between organic matter converting to amorphous carbon, and amorphous carbon formed by the initial sample heating, converting to graphite. Specific details of the chemistry in each of these steps is summarized elsewhere[37, 38] and it is likely that the true mechanism involves a complex interplay of all three steps and others not readily identifiable that might be linked to the influence of the mixed 2D and 3D structure of the matrix and the degree of porosity and its uniformity. We investigated the carbon material after pyrolysis at 400 °C using HRTEM. After initial pyrolysis, Fig. 5c confirms a mostly amorphous carbon. With laser heating at 50 mW for 10s (Fig. 5d), we observe the development of turbostratic graphitic layers with some degree of ordering and this is found the develop to reasonably well ordered, layered graphite after 10 s with 100 mW irradiation, seen in Fig. 5e. The fast Fourier transforms confirm layer development. The arcing of the FFT spots in the well-developed graphite is due to imperfect layering and stacking. These measurements directly confirm the Raman scattering and chemical decomposition mechanism whereby the carbon material continually graphitizes. Only a few regions could be found that showed ordered layering, the majority of graphitic carbon consists of a 'foam' with varied 2D and 3D layering in well-graphitized areas. It should be noted that this layered carbon disintegrates after 3 mins continued electron beam irradiation at 200 kV.

We have found that pyrolytic products from polymers are sponge-like due to the chain structure of the precursor in the amorphous solid-state matrix; the 'walls' of these sponges are comprised of quasi-layered graphite. The different morphology from the cyclic derivative **(1)** reported here confirms that the intermediate matrix formed during heating is crucial for the generation of the pyrolytic materials. Since this matrix is solid, its structure is linked to the precursor structure and decomposition mechanisms. At 800 °C the carbon content, as evident in Fig. 2c, reduces to a negligible amount confirming that the organic matter is almost completely eliminated after heating to this temperature. Conversely, the relative atomic percentage of Mn (Fig. 6) is reduced compared to that of P (*cf.* Fig. 2c) which agrees with the overall formation mechanism: the total quantity of

P from the P-containing precursor is being converted to $Mn_2P_2O_7$ while the organic matter is continually combusted.

The formation of carbon during the decarbonylation and subsequent decomposition processes was also monitored using SEM-EDAX analysis. Quantitative determination of the change in the amount of total carbon formed, both amorphous and graphitic, is shown in Fig. 6 as a function of temperature. While a graphitization process clearly occurs, it is the intermediate temperature range (300-600 °C) where the initial decomposition occurs and the final carbon content, type, and structure is found. We characteristically observe the highest C content in the range 300-400 °C. The maximum quantitative C content is found at the same temperature where the complete disappearance of the νCO bands from the cymantrene groups (Fig. 3) occurs, and as mentioned above, where the equilibrium position between organic matter decomposition and graphitization of carbon occurs.

The intermediate carbon formation is also accompanied by several changes in the morphology of the resulting inorganic phase. Although the difference between graphitic and amorphous carbon cannot be determined through FESEM, at temperatures of 400 °C and greater, a significant reduction in the density of small, high surface-to-volume ratio particles is observed. Based on the evidence, we suggest that as the carbon matrix is removed at higher temperatures, significant agglomeration and ripening of smaller crystals is now possible.

Additionally, the mechanism is influenced by the presence and formation of a stabilizing carbon, which until now was only proposed based on decomposition chemistry; this work identifies this phase, its formation and conversion to graphite during pyrolysis. The inorganic products, and nanoparticles as a pertinent example of structures formed using this approach, form at temperatures higher than their melting or boiling temperatures, which is indicative of a carbon-containing host which requires elevated temperatures due to the interfacial thermal conductivity between guest particles and host material. High interfacial thermal conductivity also prevents phase sublimation, allowing structures to form within a decomposing, but stabilizing carbon-containing host material until all that remains (Fig. 6) is the final pyrolytic product. Additionally, it has been shown that the rates of CO_2 evolution (Fig. 5a, step 1) can also influence the resulting products formed[52].

The electronic structure of the carbon matrix after pyrolysis to 600 °C was determined by NEXAFS analysis of the C 1s core level excitations. The measured core edge structure from NEXAFS spectra can be directly correlated to C 1s electronic

transitions from the C 1s core level to unoccupied states with π^* (1s $\rightarrow \pi^*$) and σ^* (1s $\rightarrow \sigma$ *) form. Figure 7 compares the NEXAFS spectra of the graphitic carbon material to that of highly oriented pyrolytic graphite (HOPG). The graphitic carbon matrix spectrum shows a smooth edge that is characteristic of a disordered sp^2-bonded matrix. The splitting of the C 1s π^* peak in the 1s $\rightarrow \pi^*$ pre-edge region in to peaks at 284.5 and 286.2 eV confirms the matrix contains two dissimilar sp^2 carbons[53]. The lower energy peak corresponds to distorted sp^2 bonds from a disordered phase. The small feature at 288.7 eV (†) stems from the presence of hydrogen and oxygen functional groups in the carbon consistent with the mechanism proposed and the detection of C-O groups and related from Raman scattering and IR analyses. The graphitic carbon matrix can thus be described as a predominantly sp^2 hybridized carbon network coexisting with a small quantity of amorphous carbon (distorted sp^2 bonds). Continued pyrolysis removes remnant sp^3 phases related to the presence of oxygen.

Our findings are in agreement with those obtained from the formation of Ag nanoparticles from thermal decomposition of silver/acetylenecarboxylic salts[54]. In that case, solid-state pyrolysis of $Ag_2(C_4O_4)$ at 300 °C leads to the formation of silver nanoparticles embedded in a carbon matrix. HRTEM analysis revealed graphitic layers surrounding the individual Ag nanoparticles. Crystalline graphite has also been observed from solution-based thermal decomposition of $Fe(COD)_2$ at 110 °C[55]. This was observed after removal with HCl of the Fe_3O_4 nanoparticles that formed.

The direct observation that graphitic carbon forms during this pyrolytic process gives further insight into the application of this new solid state strategy for nanostructure formation of metals, oxides and (pyro)phosphates. While the technique is widely applicable to any valve, noble and transition metal capable of successful coordination to an appropriate organometallic derivative of poly or cyclophosphazenes, and their mixtures, the control of nanostructure size distribution, nanostructure shape and composition etc., is likely to benefit from rational precursor design to allow cross-linking polymeric chains (from polymeric precursors to give inorganic foams) or cyclomatrix formation (from cyclic oligomeric precursors to give 2D networks of nanoparticles), and patterned deposition of the solid state precursors, which is currently under investigation.

The presence of either a carbon, or indeed and oxide-based host is important. The composition of the resulting host matrix, be it C or P_4O_7, influences the nucleation and growth of the coordinated species into separate nanoscale objects, or large porous agglomerates. Comparison to the few successful solid state strategies for nanoparticle

growth reported by Tannenbaum *et al.*[56] is that in systems where solid polymers act as the solid state phase, the rate of the formation of the metallic nanoparticles is strongly limited by the mobility, and consequently by the diffusional rates, of the growing particles in accordance with the La Mer mechanism[57] and various other growth models, including diffusion driven Ostwald ripening. Such mechanisms directly influence particle density and diffusional mobility within porous and host-material systems, and aside from the fact that this is directly dependent on the precursor design, size, molecular weight, viscosity, etc., it also relies on the formation of the thermally conductive carbonaceous host material. The solid graphitic matrix also helps to minimize large scale agglomeration; this is provided by the decomposition of the organic matter to carbon and its subsequent conversion to graphite. The ability to also form relevant tunnel-structure Li-ion battery materials using pyrophosphates (and also oxides) by this ligand free, solid state approach has specific advantages. The conductive carbon additive is formed in intimate contact with the active material in a single step and no liquids, solutions are used and the method removes issues with crystal water for sensitive lithium-containing systems and battery materials.

4. Conclusions

We have presented evidence for the formation of graphitic carbonaceous species during the intermediate annealing stages of a solid-state pyrolytic process involving trimer cyclotriphosphazenes that result in the formation of nanoparticles. Specifically, for the trimer $\{NP(OC_8H_{12})_2(OC_6H_4PPh_2\text{-}Mn(CO)_2(\eta^5\text{-}C_5H_4Me)_2\}$, evidence of intermediate carbon and graphite host matrix formation and its decomposition mechanism was confirmed by the observation of the loss of CO from the $\text{-}Mn(CO)_2$ moiety at ~320 °C in one step with the resulting $Mn_2P_2O_7$ formed as a single-crystal material. The findings confirm that the formation of metallic nanoparticles occurs within this intermediate carbon phase. In situ temperature dependent Raman scattering measurements coupled to microscopy and analytical spectroscopy, confirm several steps in the combustion process where the macromolecular precursor cleaves coordinated metals centers, undergoes decarbonylation and forms amorphous carbon, at temperatures up to 400 ºC. In-situ Raman scattering, IR and NEXAFS confirmed HRTEM evidence that carbon forms and subsequently graphitizes, with the formation and eventual elimination of C-O, C=O and other chemical groups. Subsequently, this carbon converts to a thermally conductive polycrystalline graphite matrix in which

individual crystals or pyrophosphates can form. The graphitic matrix essentially acts as a solid-state template to form a one-step composite and its thermal conductivity prevents phase sublimation. This carbon matrix can then be removed if needed by further heating to 800 ºC. The identification of graphitic carbon formation is important for the further development of this ligand-free synthetic approach for inorganic nanocrystal growth in the complete absence of liquids or solutions. For important energy storage applications, the ability to form carbon-oxide and carbon-phosphate composites in one step in the complete absence of Li- or Na-sensitive water or solutions will allow a new route to cation intercalation materials for Li-ion, Na-ion and emerging alternative batteries.

Acknowledgments

Financial support by FONDECYT (project 1085011) is gratefully acknowledged. Part of this work was conducted under the framework of the INSPIRE programme, funded by the Irish Government's Programme for Research in Third Level Institutions, Cycle 4, National Development Plan 2007-2013. This work was also supported by Science Foundation Ireland under contract no. 07/SK/B1232a.

References

1. Iijima, S., *Nature* **1991,** *354*, 56-58.
2. Geim, A. K.; Novoselov, K. S., *Nat. Mater.* **2007,** *6*, 183 - 191
3. Heer, W. A. d.; Chatelain, A.; Ugaarte, D. A., *Science* **1995,** *270*, 1179-1181.
4. Nojeh, A.; Lakatos, G. W.; Peng, S.; Cho, K.; Pease, R. F. W., *Nano Lett.* **2003,** *3*, 1469.
5. Collions, P. G.; Zettl, A.; Bando, H.; Thess, A.; Smalley, R. E., *Science* **1997,** *278*, 100-102.
6. Barros, E. B.; Demir, N. S.; Filho, A. G. S.; Filho, J. M.; Jorio, A.; Dresselhaus, G.; Dresselhaus, M. S., *Phys. Rev. B* **2005,** *71*, 165422.
7. Klett, J.; Hardy, R.; Romine, E.; Walls, C.; Burchell, T., *Carbon* **2000,** *38*, 953.
8. Dresselhaus, M.; Dresselhaus, G.; Saito, R., *Carbon* **1995,** *33*, 883-891.
9. Grobert, N., *Mater. Today* **2007,** *10*, 28-35.
10. Rao, C. N. R.; Kulkarni, G. U.; Govindaraj, A.; Satishkumar, B. C.; Thomas, P. J., *Pure Appl. Chem.* **2000,** *72*, 21-33.
11. Rao, C. N. R.; Govindaraj, A., *Acc. Chem. Res.* **2002,** *35*, 998-107.
12. Liu, Z.; Zhou, X.; Quian, Y., *Adv. Mater.* **2010,** *22*, 1-4.
13. Sen, R.; Govindaraj, A.; Rao, C. N. R., *Chem. Mater.* **1997,** *9*, 2078-2081.
14. Ma, Y.; Hu, Z.; Huo, K.; Lu, Y.; Hu, Y.; Liu, Y.; Hu, J.; Chen, Y., *Carbon* **2005,** *43*, 1667.
15. Turkevich, J., *Gold Bull.* **1985,** *18*, 86-91.
16. Brust, M.; Walker, M.; Bethee, D.; Shiffrin, D.; Whyman, R. J., *J. Chem. Soc., Chem. Commun.* **1994**, 801-802.

17. Edelstein, A. S.; Cammarata, R. C., *Nanomaterials: Synthesis Properties and Applications*. J. W. Arrowsmith Ltd: Bristol, UK, 2000.
18. Diaz, C.; Valenzuela, M. L., *Metallic Nanostructures Using Oligo and Polyphosphazenes as Template or Stabilizer in Solid State*. American Scientific Publishers 2011.
19. Petersen, R.; Foucher, D. A.; Tang, B. Z.; Lough, A.; Raju, N. P.; Greedan, J. E.; Manners, I., *Chem. Mater.* **1995,** *7*, 2045.
20. Leite, E. R.; Carreño, N. L. V.; Longo, E.; Pontes, F. M.; Barison, A.; Maniette, Y.; Varela, J. A., *Chem. Mater.* **2002,** *14*, 3722-3729.
21. Boxall, D. L.; Kenik, E. A.; Lukehart, C. M., *Chem. Mater.* **2002,** *14*, 1715-1720.
22. Wosteck, W.; Dorota, J.; Jeszka, K. J.; Amiens, C.; Chaudret, B.; Lecante, P., *J. Colloid Interface Sci.* **2005,** *287*, 107.
23. Díaz, C.; Valenzuela, M. L., *J. Inorg. Organomet. Polym. Mater.* **2006,** *16*, 211-218.
24. Díaz, C.; Valenzuela, M. L.; Zuñiga, L.; O'Dwyer, C., *J. Inorg. Organomet. Polym. Mater.* **2009,** *19*, 507-520.
25. Diaz, C.; Valenzuela, M. L.; Bravo, D.; Lavayen, V.; O'Dwyer, C., *Inorg. Chem* **2008,** *47*, 11561-11569.
26. Díaz, C.; Valenzuela, M. L.; Spodine, E.; Moreno, Y.; Peña, O., *J. Cluster Sci.* **2007,** *18*, 831-844.
27. Jimenez, J.; Laguna, A.; Benouazzane, M.; Sanz, J. A.; Díaz, C.; Valenzuela, M. L.; Jones, P. G., *Chem. Eur. J.* **2009**, 13509-13520.
28. Diaz, C.; Valenzuela, M. L.; Laguna, A.; Lavayen, V.; Jimenez, J.; Power, L.; O'Dwyer, C., *Langmuir* **2010,** *26*, 10223-10233.
29. Diaz, C.; Lavayen, V.; O'Dwyer, C., *J. Solid State Chem.* **2010,** *183*, 1595-1603.
30. Finney, E. E.; Finke, R. G., *J. Colloid Interface Sci.* **2008,** *317*, 351-374.
31. Skrdla, P. J.; Robertson, R. T., *Chem. Mater.* **2008,** *20*, 3.
32. Philipe, L.; Michler, J., *Small* **2008,** *4*, 904-907.
33. Goia, D. V., *J. Mater. Chem.* **2004,** *14*, 451-458.
34. Capek, I., *Adv. Coll. Interface Sci.* **2004,** *110*, 49-74.
35. Tadd, E.; Zeno, A.; Zubris, M.; Dan, N.; Tannenbaum, R., *Macromolecules* **2003,** *36*, 6497-6502.
36. Hautier, G.; Jain, A.; Ong, S. P.; Kang, B.; Moore, C.; Doe, R.; Ceder, G., *Chem. Mater.* **2011,** *23*, 3495-3508.
37. Carriedo, G.; Garcia-Alonso, F. J.; González, P. A.; Díaz, C.; Yutronic, N., *Polyhedron* **2002,** *21*, 2579-2586.
38. Diaz, C.; Valenzuela, M. L.; Bravo, D.; Lavayen, V.; O'Dwyer, C., *J. Colloid Interface Sci.* **2011,** *362*, 21-32.
39. Díaz, C.; Valenzuela, M. L., *J. Inorg. Organomet. Polym. Mater.* **2006,** *16*, 123-128.
40. Díaz, C.; Carriedo, G. A.; Valenzuela, M. L., *Polymer Bull.* **2009,** *63*, 829-835.
41. Endo, M.; Nishimura, K.; Kim, Y. A.; Hakamada, K.; Matushita, T.; Dresselhaus, M. S.; Dresselhaus, G., *J. Mater. Res.* **1999,** *14*, 4474-4477.
42. Nemanich, R. J.; Solin, S. A., *Phys. Rev. B* **1979,** *20*, 392-401.
43. Campos-Delgado, J.; Farhat, H.; Kim, Y. A.; Reina, A.; Kong, J.; Endo, M.; Muramatsu, H.; Hayashi, T.; Terrones, H.; Terrones, M.; Dresselhaus, M. S., *Small* **2009,** *5*, 2698-2702.
44. Tang, C.; Wooley, K. K.; Matyjaszewski, K.; Kowalewski, T., *Angew. Chem. Int. Ed.* **2004,** *43*, 2783-2787.
45. Lee, K. T.; Ji, X.; Rault, M.; Nazar, L., *Angew. Chem. Int. Ed.* **2009,** *48*, 1-6.

46. Dresselhaus, M. S.; Jorio, A.; Hofmann, M.; Dresselhaus, G.; Saito, R., *Nano Lett.* **2010,** *10*, 751-758.
47. Dresselhaus, M. S.; Dresselhaus, G.; Jorio, A.; Filho, A. G. S.; Pimenta, M. A.; Saito, R., *Acc. Chem. Res.* **2002,** *35*, 1070-1078.
48. Cancado, L. G.; Pimenta, M. A.; Saito, R.; Jorio, A.; Ladeira, L. O.; Grueneis, A.; Souza-Filho, A. G.; Dresselhaus, G.; Dresselhaus, M. S., *Phys. Rev. B* **2002,** *66*, 035415.
49. Ferrari, A. C.; Robertson, J., *Phil. Trans. R. Soc. Lond. A* **2004,** *362*, 2477-2512.
50. Tuinstra, F.; Koenig, J. L., *J. Chem. Phys.* **1970,** *53*, 1126-1130.
51. Matthews, M. J.; Pimenta, M. A.; Dresselhaus, G.; Dresselhaus, M. S.; Endo, M., *Phys. Rev. B* **1999,** *59*, R6585-R6588; O'Dwyer, C.; Lavayen, V.; Ana, M. A. S.; Benavente, E.; González, G.; Torres, C. M. S. *J. Electrochem. Soc.* **2007,** *154*, K29.
52. Park, J.; Joo, J.; Kwon, S. G.; Jang, Y.; Hyeon, T., *Angew. Chem. Int. Ed.* **2007,** *46*, 4630-4660.
53. Tang, Y. H.; Zhang, P.; Kim, P. S.; Sham, T. K.; Hu, Y. F.; Sun, X. H.; Wong, N. B.; Fung, M. K.; Zheng, Y. F.; Lee, C. S.; Lee, S. T., *Appl. Phys. Lett.* **2001,** *79*, 3773.
54. Dallas, P.; Bourlinos, A. B.; Komninou, P.; Karakassides, M.; Niarchos, D., *Nanoscale Res. Lett.* **2009,** *4*, 1381-1388.
55. Walker, E. C.; Beetz, T.; Sfeir, M. Y.; Brus, L. E.; Steigerwald, M. L., *J. Am. Chem. Soc.* **2006,** *128*, 15590-15591.
56. Rotstein, H. G.; Novick-Cohen, A.; Tannenbaum, R., *J. Stat. Phys.* **1998,** *90*, 119-143.
57. LaMer, V. K.; Dinegar, R. H., *J. Am. Chem. Soc.* **1950,** *72*, 4847-4847.

Figure captions

Scheme 1 Schematic representation of the solid-state method for the synthesis of nanostructured materials from oligomeric and polymeric precursors.

Scheme 2 Schematic representation of the proposed solid state mechanism of nanoparticle formation. Continual polymeric or trimeric decomposition occurs during pyrolysis resulting in crystals aggregation and ripening of cleaved metallic centers in a graphitizing carbon matrix.

Fig. 1 Schematic representation of $\{NP(OC_8H_{12})_2(OC_6H_4PPh_2\text{-}Mn(CO)_2(\eta^5\text{-}C_5H_4Me)_2\}$ **(1)**.

Fig. 2 (a) X-ray diffraction analysis of the $Mn_2P_2O_7$ (ICDD, No. 29-0891) crystalline product from pyrolysis of $NP(OC_8H_{12})_2(OC_6H_4PPh_2\text{-}Mn(CO)_2(\eta^5\text{-}C_5H_4Me)_2$. Arrows highlight $Mn_2P_2O_7$ peaks and * marks the (002) diffraction from graphite. (b) Corresponding survey scanning electron microscopy image of the pyrolytic product. (c)

Energy dispersive X-ray analysis of the products confirming the presence of Mn, P, O, and C. (d) TEM analysis of crystalline particles and structures formed during pyrolysis. (e)

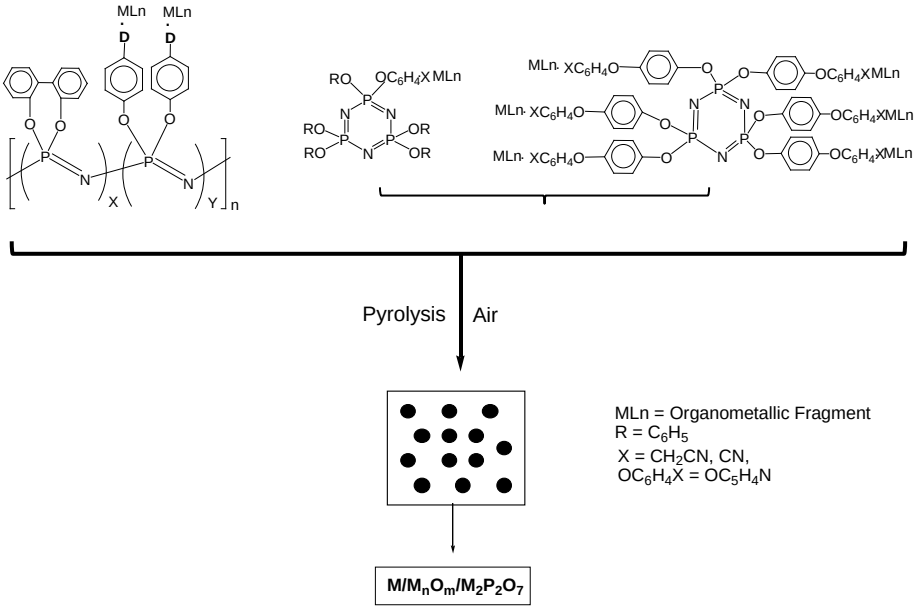
Fig. 3 FTIR spectra in the wavenumber region 2000-1600 cm^{-1} from the pyrolytic product from $NP(OC_8H_{12})_2(OC_6H_4PPh_2\text{-}Mn(CO)_2(\eta^5\text{-}C_5H_4Me)_2$ acquired at temperatures in the range 250 – 400 °C.

Fig. 4 (a-c) Raman spectra of the pyrolysis product acquired at a constant temperature of 400 °C at several laser powers. (d) I_D/I_G ratios for the pyrolytic product as a function laser power acquired at constant temperatures of 400 and 600 °C.

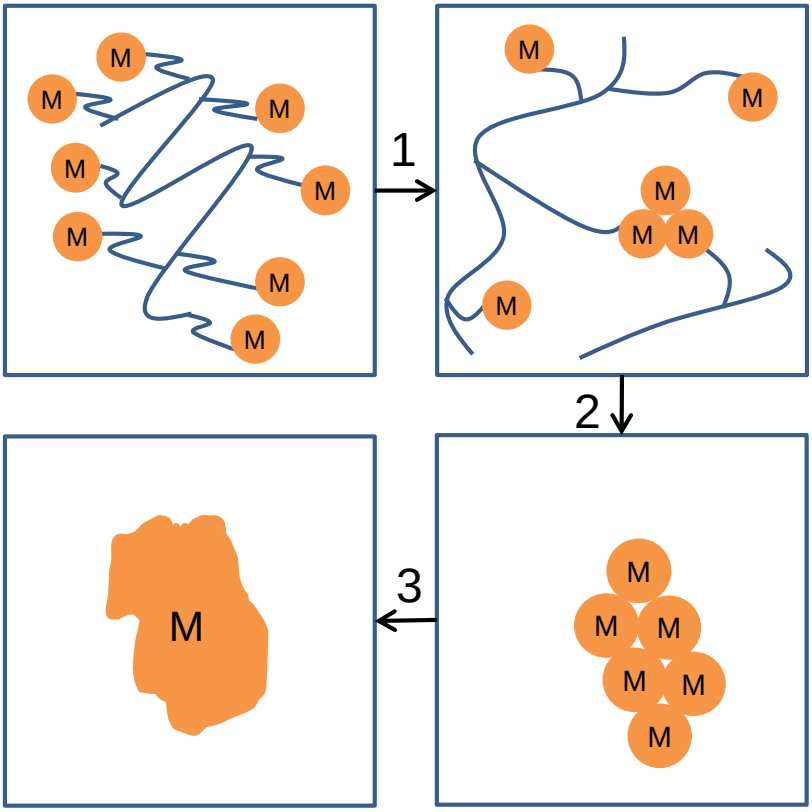
Fig. 5 Schematic representation of carbon and its graphitization during the pyrolysis of the precursor. (a) Optional paths for the combustion and graphitization of the carbon formed during trimeric decomposition. (b) Nanomaterial seeds and forms within the carbon host with the final nanomaterial lodged within a mostly graphite host material. (c) HRTEM image of the carbon material after pyrolysis at 400 °C and corresponding HRTEM images for pyrolyzed carbon after laser heating at (d) 50 mW for 10s and (e) layered graphitic carbon after 100 mW irradiation for 10 s.

Fig. 6 EDAX analysis for the pyrolytic product measured after pyrolysis to temperatures in the range 300 – 400 °C. (Insets) Corresponding SEM images of the C-pyrolytic product in the same temperature range. Scale bar = 70 μm.

Fig. 7 (a) NEXAFS spectra of the carbon K-edge from (a) the carbon matrix after pyrolysis and (b) HOPG. (c) Normalized NEXAFS spectrum of the oxygen K-edge from the pyrolytic carbon sample.


MLn
D
MLn
D
O
O
O
O
P
N
P
N
X
Y
n
RO
OC6H4X MLn
N
P
N
RO
P
OR
RO
N
P
OR
MLn XC6H4O
O
O
OC6H4XMLn
MLn XC6H4O
O
N
P
N
O
OC6H4XMLn
MLn XC6H4O
O
P
N
P
O
OC6H4XMLn
Pyrolysis
Air
MLn = Organometallic Fragment
R = C6H5
X = CH2CN, CN,
OC6H4X = OC5H4N
M/MnOm/M2P2O7

Scheme 1



Scheme 2

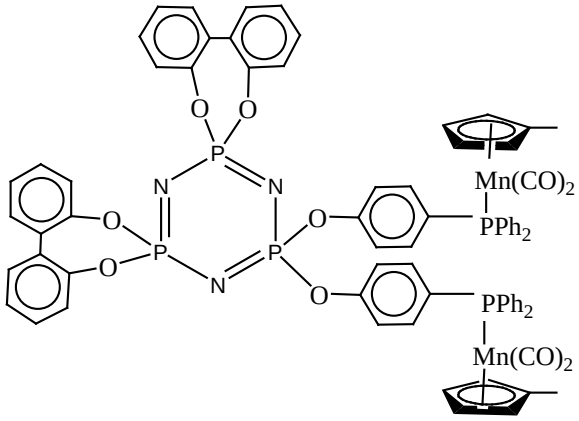


Figure 1

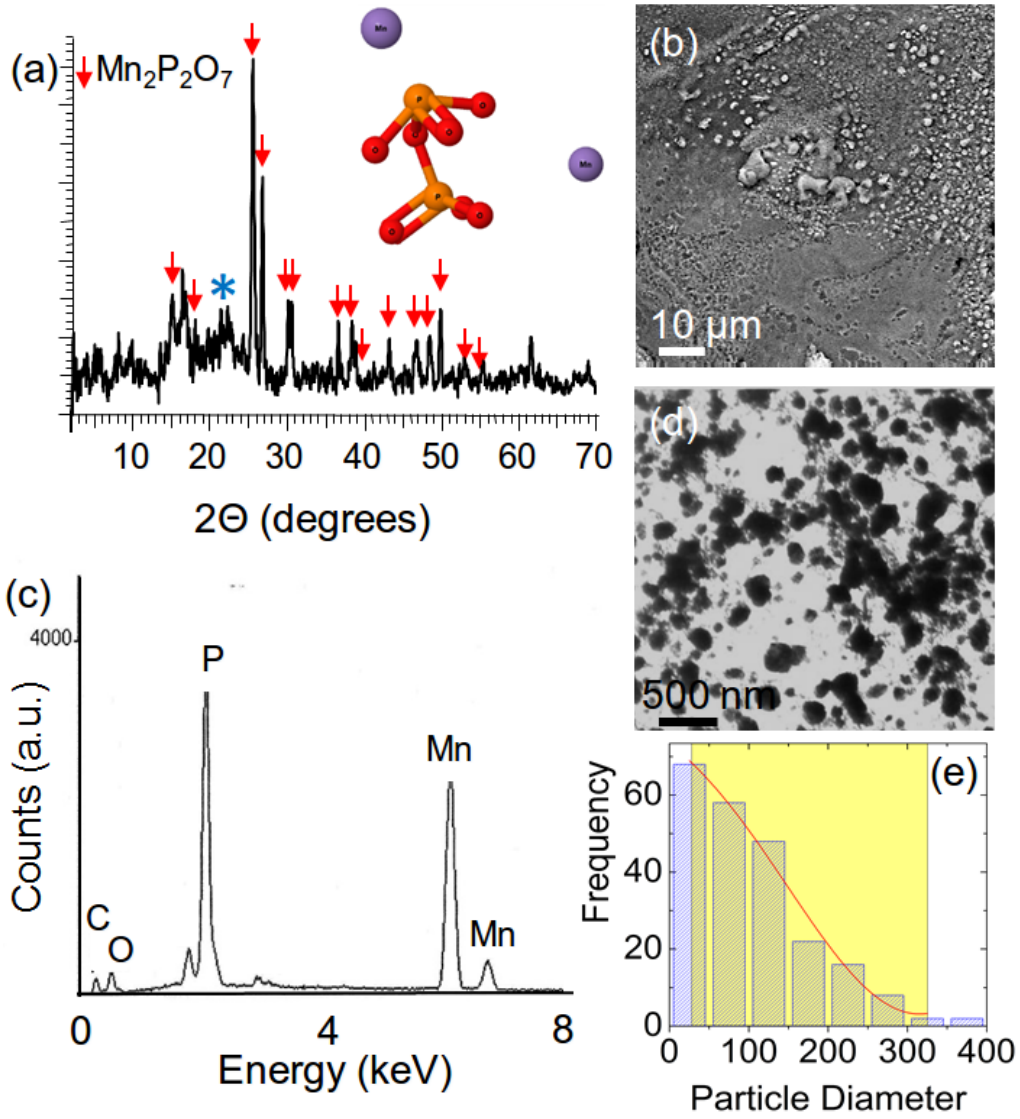

(a)
$Mn_2P_2O_7$
10
20
30
40
50
60
70
2Θ (degrees)
(b)
10 μm
(d)
500 nm
(c)
4000
Counts (a.u.)
P
Mn
C
O
Mn
0
4
8
Energy (keV)
(e)
Frequency
60
40
20
0
0
100
200
300
400
Particle Diameter

Figure 2

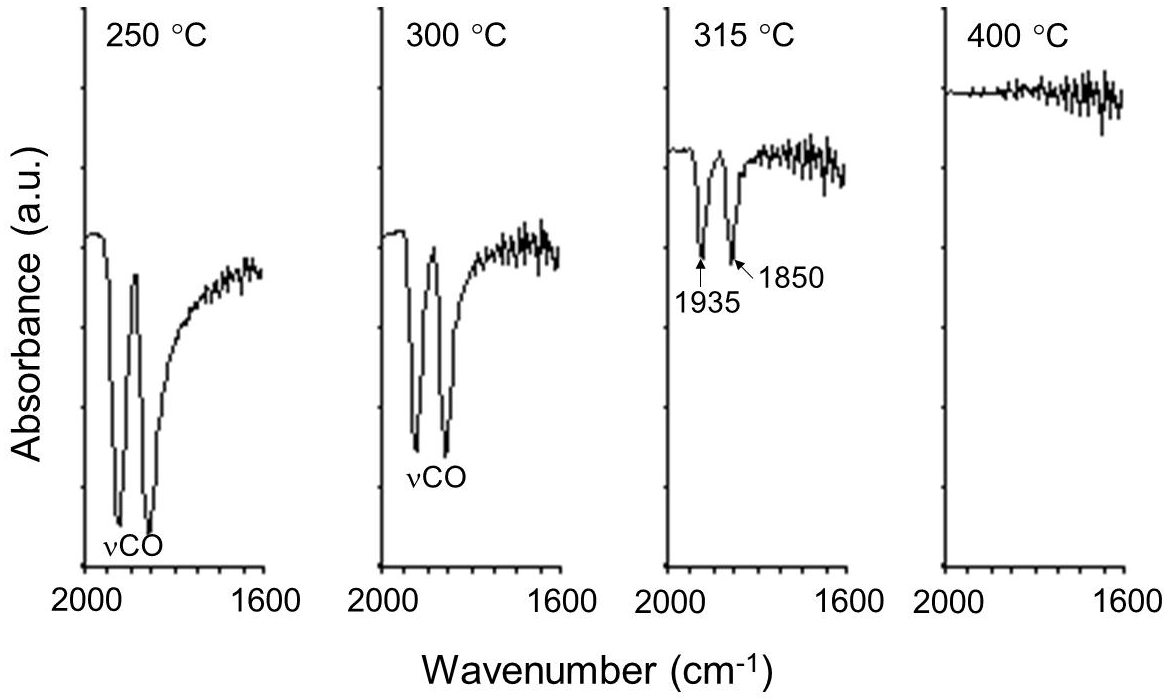

250 °C
300 °C
315 °C
400 °C
Absorbance (a.u.)
νCO
νCO
1935
1850
2000
1600
2000
1600
2000
1600
2000
1600
Wavenumber (cm-1)

Figure 3

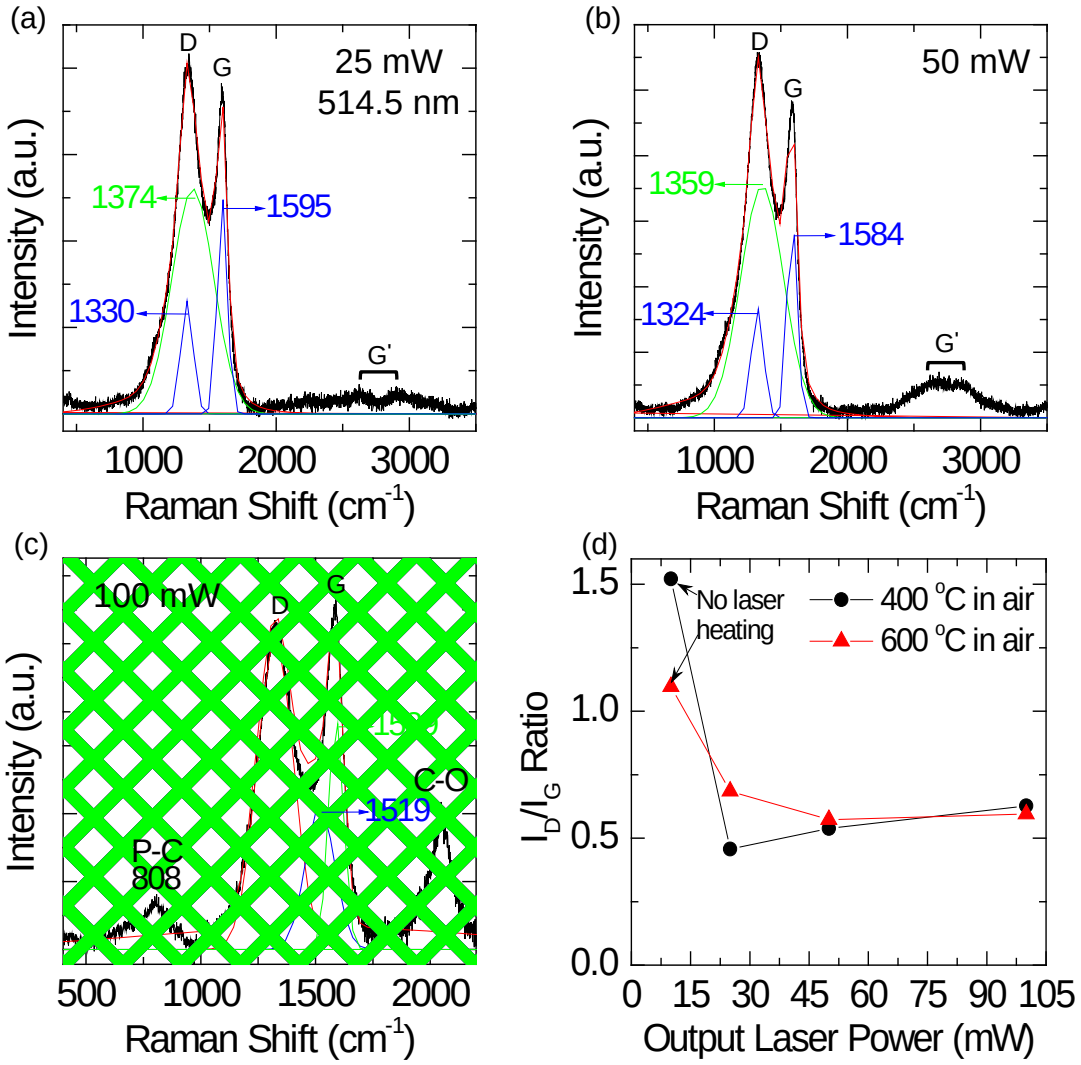

(a)
D
G
25 mW
514.5 nm
1374
1595
1330
G'
Intensity (a.u.)
1000
2000
3000
Raman Shift (cm-1)
(b)
D
G
50 mW
1359
1584
1324
G'
Intensity (a.u.)
1000
2000
3000
Raman Shift (cm-1)
(c)
100 mW
D
G
C-O
1519
P-C
808
Intensity (a.u.)
500
1000
1500
2000
Raman Shift (cm-1)
(d)
No laser
heating
400 °C in air
600 °C in air
ID/IG Ratio
1.5
1.0
0.5
0.0
0
15
30
45
60
75
90
105
Output Laser Power (mW)

Figure 4

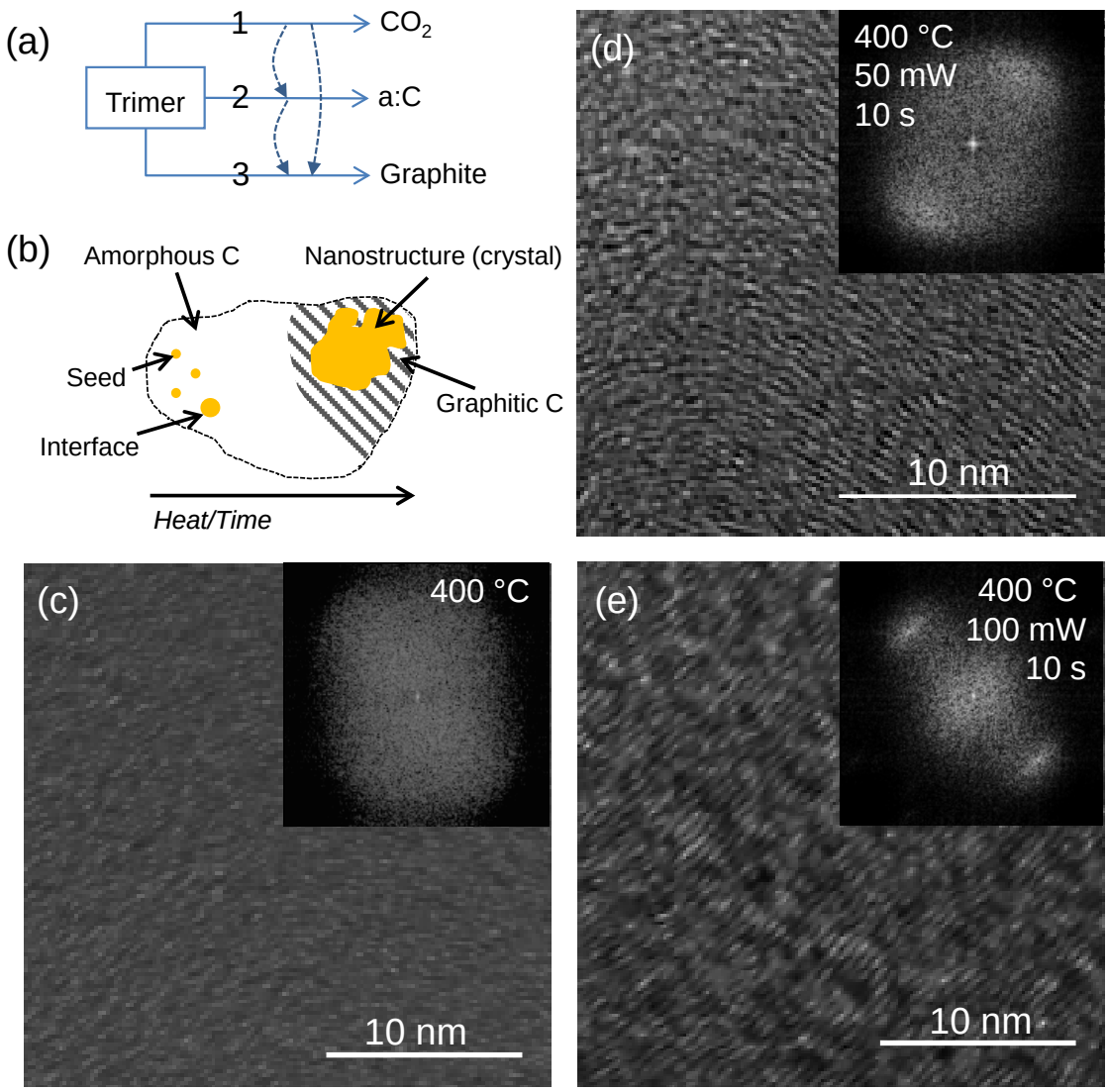

(a)
Trimer
1
2
3
CO_2
a:C
Graphite
(b)
Amorphous C
Nanostructure (crystal)
Seed
Interface
Graphitic C
Heat/Time
(d)
400 °C
50 mW
10 s
10 nm
(c)
400 °C
10 nm
(e)
400 °C
100 mW
10 s
10 nm

Figure 5

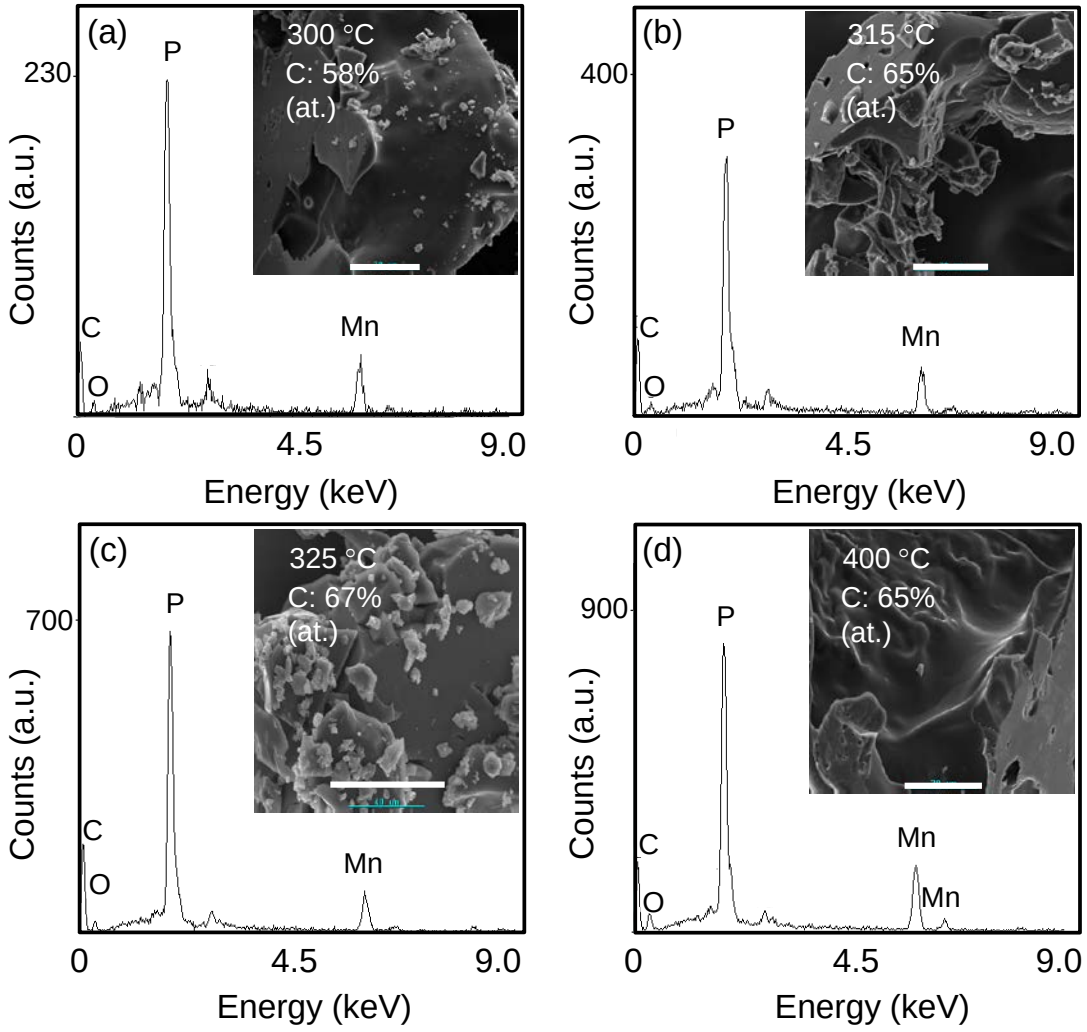

(a)
300 °C
C: 58%
(at.)
P
C
O
Mn
230
Counts (a.u.)
0
4.5
9.0
Energy (keV)
(b)
315 °C
C: 65%
(at.)
P
C
O
Mn
400
Counts (a.u.)
0
4.5
9.0
Energy (keV)
(c)
325 °C
C: 67%
(at.)
P
C
O
Mn
700
Counts (a.u.)
0
4.5
9.0
Energy (keV)
(d)
400 °C
C: 65%
(at.)
P
C
O
Mn
Mn
900
Counts (a.u.)
0
4.5
9.0
Energy (keV)

Figure 6

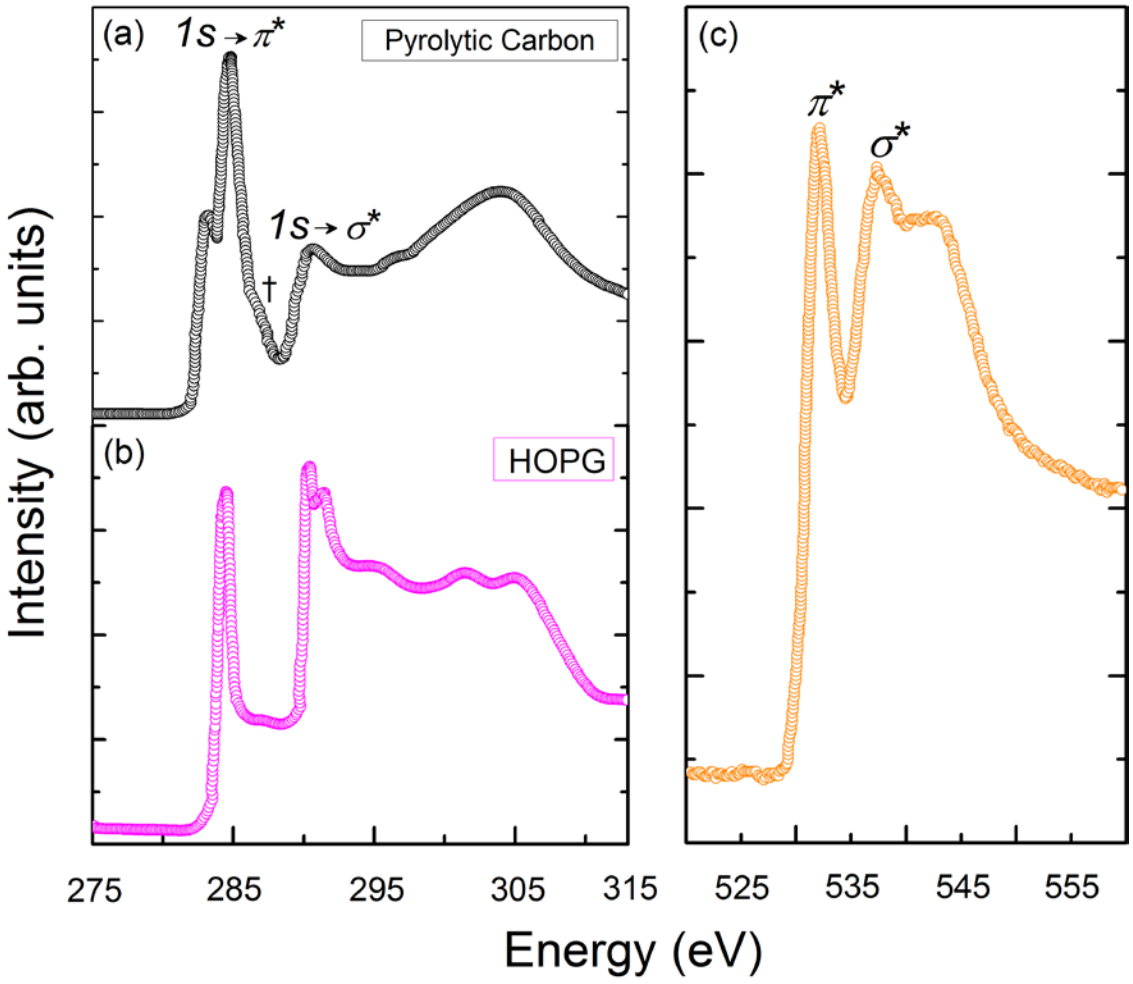

(a) 1s→π*
Pyrolytic Carbon
1s→σ*
†
(b)
HOPG
(c)
π*
σ*
Intensity (arb. units)
275
285
295
305
315
525
535
545
555
Energy (eV)

Figure 7